ORNL/TM-2020/1659

Physical and Thermomechanical Properties of Yttrium Hydride from Large Scale Bulk Metal Hydriding Furnace

Xunxiang Hu
Danny Schappel
Artem A. Trofimov
Hsin Wang
Ying Yang
Chinthaka M. Silva
Mehdi Balooch
Kurt A. Terrani

September 2020

M2TC-20OR0406015

OAK RIDGE NATIONAL LABORATORY
MANAGED BY UT-BATTELLE FOR THE US DEPARTMENT OF ENERGY

ORNL/TM-2020/1659

Transformational Challenge Reactor Program

PHYSICAL AND THERMOMECHANICAL PROPERTIES OF YTTRIUM HYDRIDE FROM LARGE SCALE BULK METAL HYDRIDING FURNACE

Xunxiang Hu, Danny Schappel, Artem A. Trofimov, Hsin Wang, Ying Yang, Chinthaka M. Silva, Kurt A. Terrani

Oak Ridge National Laboratory

Mehdi Balooch

University of California, Berkeley

Date Published: September 2020

M2TC-20OR0406015

Prepared by
OAK RIDGE NATIONAL LABORATORY
Oak Ridge, TN 37831-6283
managed by
UT-BATTELLE, LLC
for the
US DEPARTMENT OF ENERGY
under contract DE-AC05-00OR22725

CONTENTS

LIST OF FIGURES

LIST OF TABLES

ACRONYMS

ANP	Aircraft Nuclear Propulsion
ASTM	American Society for Testing and Materials
CTE	Coefficient of linear thermal expansion
DOE	US Department of Energy
DSC	Differential scanning calorimeter
EBSD	Electron Backscatter Diffraction
FCC	Face Centered Cubic
HCP	Hexagonal Closest Packed
LAMDA	Low Activation Materials Development and Analysis laboratory
LFA	Laser Flash Technique
ORNL	Oak Ridge National Laboratory
PCT	Pressure-Composition-Temperature map
SEM	Scanning electron microscope
SNAP	Systems Nuclear Auxiliary Power
SRM	Standard reference material
TRIGA	Training, Research, Isotopes, General Atomic
TCR	Transformational Challenge Reactor
XRD	X-ray Diffraction
YH_x	Yttrium Hydride
ZrH_x	Zirconium Hydride

ACKNOWLEDGMENTS

This research was supported by the Transformational Challenge Reactor program supported by the US Department of Energy, Office of Nuclear Energy. The report was authored by UT-Battelle under Contract No. DE-AC05-00OR22725 with the DOE.

The authors also thank Ben Garrison at ORNL for the assistance with the fabrication of the yttrium hydride and his technical review of the report. We thank Dr. T.S. Byun for the technical review.

ABSTRACT

Given the superior thermal stability and highly attainable hydrogen density, yttrium hydride is an excellent high-temperature moderator material in advanced thermal neutron spectrum reactors that require small core volumes. Yttrium hydride has been selected as the moderator material for the Transformational Challenge Reactor, which was launched at Oak Ridge National Laboratory (ORNL) in 2019. However, fabrication of large-scale crack-free yttrium hydride is challenging and very limited efforts have been committed to the characterization of bulk yttrium hydride in response to the need to establish a complete database of the thermomechanical properties of YH_x. In this report, the challenges associated with fabricating large-scale crack-free yttrium hydride are discussed herein. In response to those challenges, a hydriding system was designed and constructed at ORNL and was used to successfully fabricate crack-free yttrium hydride in complex geometries at large scales. This was accomplished by precisely controlling the hydrogen's partial pressure and the retort temperature, which was informed by the well-established thermodynamic properties of the binary H-Y system. Hydrogen content in as-fabricated hydride was determined by the weight change method and vacuum hot extraction technique, complemented by the X-ray diffraction (XRD). In addition, significant efforts are being dedicated to establishing a complete database of the thermomechanical properties of as-fabricated yttrium hydride. In FY2020, we investigated the thermophysical properties of yttrium hydrides as a function of temperature (room temperature to 700°C) and hydrogen concentration (H/Y ratio ranges from 1.52 to 1.93). The results indicate that at the temperatures below 300 °C, the hydrogen content did not have a significant influence on the thermal expansion, while the specific heat capacity, the thermal diffusivity, and the calculated thermal conductivity were slightly higher for the higher H/Y ratio. Between 300°C and 700 °C, a reversible second-order endothermic transition in all measured thermal properties was observed. It was also found that the onset temperatures of the observed transition varied, with the composition having inverse dependence on the hydrogen content. An attempt was made to explain the behavior of the thermophysical properties at higher temperatures by considering the order–disorder transition as a result of hydrogen redistribution. In addition, nanoindentation was employed to determine the elastic modulus and hardness and to capture the crystal orientation dependence of these parameters. Vickers hardness was also reported. The final section of the report introduces ongoing neutron irradiation campaign of yttrium hydride.

1. INTRODUCTION

Hydrogen has broad applications in both nuclear and non-nuclear systems [1, 2]. Hydrogen is an outstanding moderator for fast neutrons in nuclear systems because of the equivalent mass to the neutron, the low neutron absorption cross section, and the acceptably high neutron scattering cross section [1, 3]. Given the high energy density, hydrogen is also an ideal energy carrier [4]. Metal hydrides have been recognized as an efficient, low-risk option for high-density hydrogen storage since the late 1970s [1]. As to the nuclear application, metal hydrides are particularly well suited for use in thermal reactor systems in which core weight and volume must be minimized. In thermal reactor systems, metal hydrides serve as a constituent in fuels and in moderator and shield materials. ZrH_x in the form of the matrix for fissile materials—U(30wt%)-$ZrH_{1.6}$—was employed as the moderator material in the Systems Nuclear Auxiliary Power (SNAP) Program [5], Training, Research, Isotopes, General Atomic (TRIGA) research reactors [6], and nuclear thermal propulsion reactors [7]. Higher power density, high moderator density inherent to the fuel, large prompt negative fuel-temperature reactivity feedback, and higher thermal conductivity are attractive attributes of this class of hydride fuels [6]. Hexagonal cross section rods of clad YH_x were investigated for possible application as moderator elements in the gas-cooled Aircraft Nuclear Propulsion (ANP) reactor developed by General Electric [3, 8]. In addition to the outstanding neutron moderating characteristics, hydrogen, particularly as a metal hydride, offers other unique nuclear advantages when used as a shield component. The desirable elements of an ideal nuclear reactor shield are hydrogen for neutron moderation and a heavy metal effectively absorbing gamma-ray. However, the high cost limited the metal hydride's application as a radiation shield. Metal hydrides were also proposed for use in reactivity control elements for fast-spectrum nuclear reactors to facilitate thermalization and subsequent absorption of neutrons [9]. Furthermore, variation of hydride temperature would provide attendant reversible changes in the equilibrium concentration of hydrogen, affecting and reducing the reactivity [10].

In contrast to ZrH_x and other metal hydrides under consideration as moderator, YH_x offers unique advantages as a moderator for high-temperature thermal neutron spectrum reactors, even though ZrH_x has lower neutron absorption cross section and consequentially a higher moderating ratio. YH_x exhibits superior thermal stability and retains relatively high content of hydrogen at elevated temperatures [1, 11]. This is particularly true at temperatures above 870°C. For example, when in equilibrium with 1 atm H_2 at 900°C and 1,100°C, the attainable hydrogen content in yttrium hydride is 1.6 and 2.6 times that in zirconium hydride, respectively. The equilibrium hydrogen pressure of YH_x is several orders of magnitude lower when compared to ZrH_x with the same hydrogen/metal atomic ratio at the same temperature. This also illustrates the ability of YH_x to retain hydrogen at elevated temperatures. In contrast, the application of ZrH_x in nuclear systems has required careful management of the moderator temperature and additional effort to develop a hydrogen barrier (e.g, metal cladding or self-protecting oxide or nitride layers on the surface of the hydride itself) to mitigate hydrogen desorption at elevated temperatures [3]. The development of hydrogen barriers for YH_x becomes necessary when the hydrogen loss at elevated temperatures is unacceptable. Although the YH_x moderator is attractive, in the nuclear systems of the first nuclear era, the unavailability of high-purity yttrium as an industrial metal and its prohibitive cost—30 times the cost of metal zirconium [12]—did not allow for the broad application [13]. However, high-purity yttrium is now widely available as a commercial product at an affordable price, even at the ultra–high-purity grade of 99.9%, which is <$50/kg [14]. Therefore, the time is ripe to reap the benefits of this metal hydride to enable advanced nuclear energy applications.

YH_x is now being developed under various US Department of Energy (DOE) programs to serve as the moderator for microreactors and small modular reactors, which have wide civilian applications because of their capabilities to be deployed with low enriched uranium and integrated with microgrids [15]. DOE's Office of Nuclear Energy launched the TCR program in 2019 to build and operate an additively manufactured microreactor at Oak Ridge National Laboratory (ORNL). The TCR program aims to

demonstrate a faster, more affordable approach to advanced nuclear energy [16]. YH_x was selected as the moderator material for this reactor [17].

Based on these various proposed applications in nuclear systems, it is manifest that there is a high demand for large-scale, crack-free bulk YH_x. Fabrication of metal hydrides is usually achieved through the direct reaction of metals and hydrogen at elevated temperatures in a Sieverts' high vacuum apparatus. Considerable difficulty was encountered due to cracks forming in the fabricated yttrium hydride [3, 8] in the ANP program of the 1960s. The cracks were associated with the large amount of impurities in the starting yttrium metals. Houten [12, 18, 19] demonstrated that including additives, which are usually present as carbides or borides, allowed for achieving small metal grain size, and the carefully tuned hydriding cycle yielded crack-free hydride bodies. After nearly 30 years of dormancy in yttrium hydride fabrication and characterization, crack-free, small YH_x samples were successfully fabricated by a Japanese research group using an ultra-high vacuum Sieverts' apparatus [20, 21] to investigate the thermomechanical properties of this material as a function of hydrogen concentration. Large-scale yttrium hydride may also be fabricated via the powder sintering route, as demonstrated by researchers at Los Alamos National Laboratory [22].

In addition to the fabrication of crack-free yttrium hydride, very limited efforts have been committed to the characterization in response to the need to establish a complete database of the thermomechanical properties of YH_x to facilitate its deployment as high temperature moderator. Preliminary evaluation of the thermomechanical properties of YH_x were carried out in 1960s and available in Ref. [1]. Since the availability of high purity yttrium, Ito et al [21] reported the thermal properties (i.e., specific heat capacity, thermal diffusivity, and thermal conductivities) of three bulk yttrium hydride samples ($YH_{1.72}$, $YH_{1.86}$, and $YH_{1.90}$) in the temperature range from 300 to 773K. Setoyama et al from the same research group [20] investigated Vickers hardness and Young's modulus of YH_x ($1.7<x<2.0$) at room temperature. In addition to the bulk yttrium hydride, Shivprasad et al [11] reported the elastic moduli of high-density sintered monoliths of yttrium dihydride. However, a reliable database of YH_x properties as a function of hydrogen concentration remains incomplete.

This report summarized the R&D activities under Hydride Thrust of the TCR program, including the fabrication of the crack-free yttrium hydride by using the TCR large scale bulk metal hydriding furnace [23] and the thermomechanical property measurements.

2. FABRICATION OF BULK CRACK-FREE YTTRIUM HYDRIDE

2.1 CHALLENGES ASSOCIATED WITH FABRICATING BULK CRACK-FREE YTTRIUM HYDRIDE

Yttrium hydrides with the desired H/Y atomic ratios can be fabricated in a variety of ways: such as introducing a measured amount of hydrogen into small-volume retorts or carefully matching retort temperature and hydrogen pressure. The Y-H binary phase diagram and the pressure-composition-temperature (PCT) map are the two most important pieces of information needed to guide fabrication of yttrium hydride. A reliable thermodynamics database of the Y-H binary system was gradually established once ultra–high-purity yttrium metal became available in the late 1970s [24-27], even though significant effort had been expended in the 1960s to investigate this binary system [28, 29].

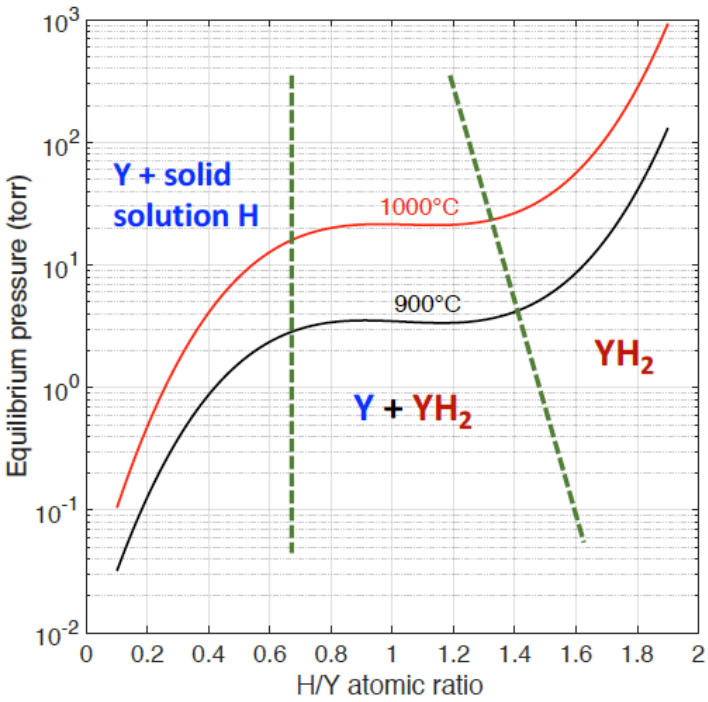

Figure 1. Equilibrium hydrogen partial pressure of the Y-H binary phase as a function of the H/Y atomic ratio at 900°C and 1,000°C, respectively, predicted by using data adapted from Begun et al. [24].

Based on the PCT curves [24], the experimental isotherms of the Y-H system basically describe the phase evolution during the hydriding process. As shown in Figure 1, the logarithm of the equilibrium hydrogen pressure first increases approximately linearly with the H/Y atomic ratio. In this region, only the metal phase exists: an interstitial solid solution of atomic hydrogen in metal Y with ample solubility. Then, as the concentration of dissolved hydrogen is increased, the equilibrium hydrogen pressure reaches a plateau, and the curve becomes relatively flat. This marks the onset of the two-phase region in which H activity is at equilibrium between (1) the solid solution of atomic hydrogen in metal yttrium and (2) a hydrogen-deficient face-centered cubic (FCC) YH_{2-x} phase. With the addition of more hydrogen and a corresponding increase of the YH_{2-x} phase fraction, the curve starts to slope upward, indicating that all the metal has been consumed, and only a single-phase region exists once again: the slightly hydrogen-deficient δ phase yttrium hydride. However, the experimental data in the temperature range of >1,000°C and in the atomic ratio of H/Y>1.90 are not yet available. The thermodynamics properties of YH_x at higher temperatures and the hydrogen contents can be obtained by extrapolating from the data that are currently available.

Hydriding is a rate-controlled exothermic process [1]. The rate limiting process may be diffusion of hydrogen inside the solid metal or hydride, as H is supplied to the solid or surface adsorption, depending on the bulk H_2 gas flux onto the surface. Phase transformation of the metal to hydride (or vice versa) is a moving boundary growth process similar to what occurs in Zr-H system [30]. However, the interfacial reaction rate is not deemed as rate limiting. The most significant challenge in fabricating massive crack-free bulk metal hydride (or during rapid dehydriding) is that if the hydrogen concentration gradient across the sample body is not managed to a low value, then differential lattice strain results, leading to significant stress. This stress, coupled with the low fracture toughness of the hydride materials, is the ultimate cause of cracking, and it is routinely exploited to produce powder from various metals in the hydride-dehydride process. In this work, finite element analysis was performed using BISON [31] to semi-quantitatively demonstrate the stress distribution in an yttrium sphere of 1 mm in diameter under various hydrogen concentration gradients along the radial direction. The simulation temperature was set to 823K, and it remained constant without considering the exothermic nature of the hydriding process. The swelling of

yttrium hydride was assumed to be proportional to the H/Y atomistic ratio. The swelling was 7.1 % at $YH_{1.8}$ and 0 for Y, linearly increasing between these values. The elastic modulus was set to 66 GPa for Y and 140 GPa for $YH_{1.84}$ [20], linearly increasing with hydrogen concentration. Poisson's ratio was set to a constant 0.27. The densities of yttrium and yttrium hydride were set to 4,500 and 4,200 kg/m^3, respectively [32]. A linear correlation between density and the H/Y ratio was assumed. Four cases were evaluated: (a) the H/Y atomic ratio as 0 for radii less than 0.21 mm and 1.84 otherwise; (b) the H/Y ratio linearly increasing for radii greater than 0.21 mm from 0 to 1.84; (c) the hydrogen concentration following a linear gradient through the radius from 0 to 1.84; and (d) the H/Y ratio linear increasing from 1.74 to 1.84, starting from the radius of 0.

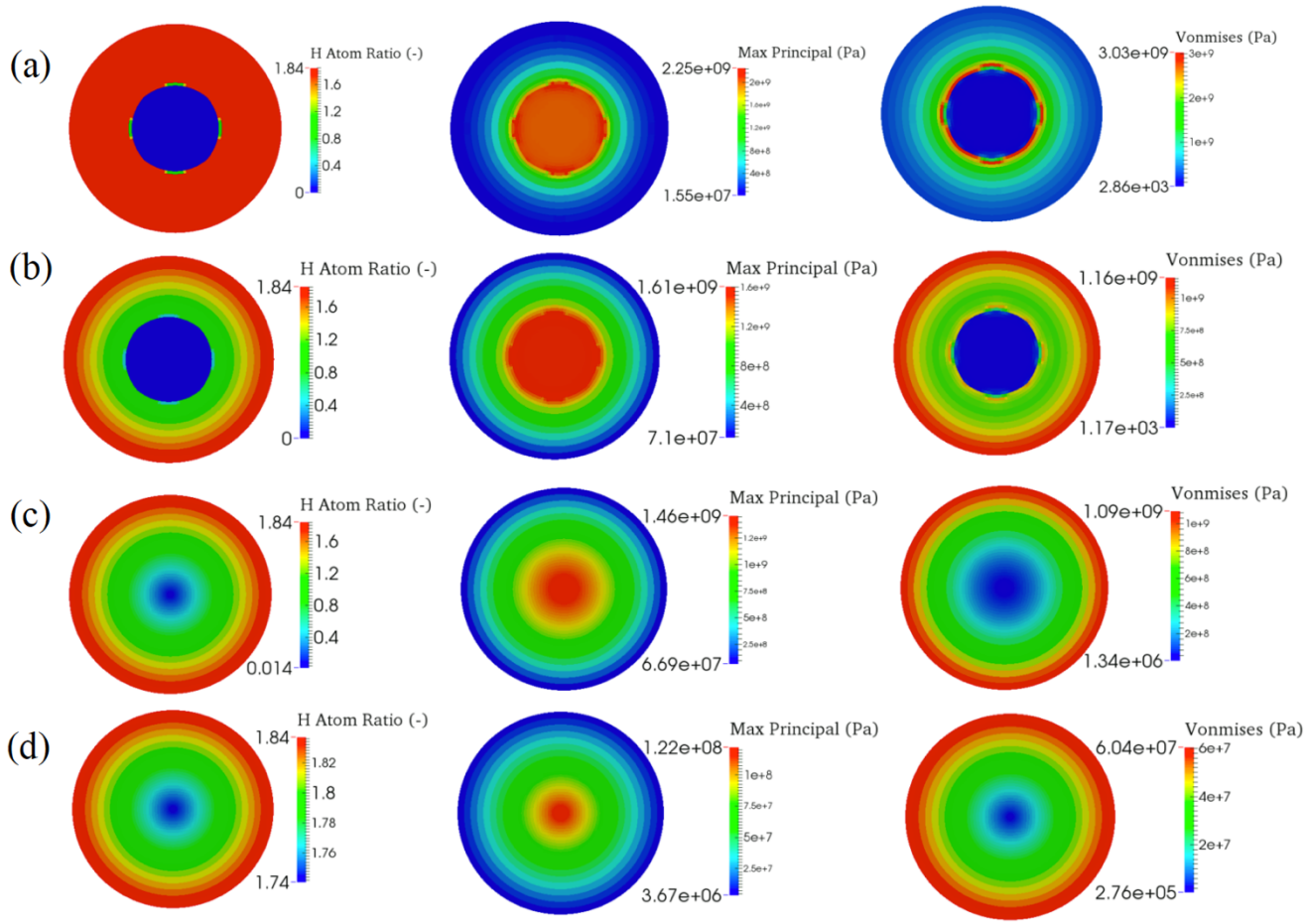

Figure 2. The hydrogen concentration gradient, the maximum principal stress, and the von Mises stress distribution for four distinct H concentration profiles. The H concertation gradients (left) become more gradual and flat moving from scenario (a) to (d), resulting in the lower stresses arising from lattice differential strain (right) [23].

Figure 2 shows the hydrogen concentration gradient, the maximum principal stress (relevant when assessing brittle hydride), and the von Mises stress (relevant for assessing ductile metal) distribution in each case. In the first three simulations, significant stress built up within the spherical sample, and Case 1, with the sharpest hydrogen concentration, had the highest stress. The yttrium hydride perimeter swelled and attempted to pull the yttrium core outward. Thus, the yttrium hydride region was subjected to strong compressive hoop stress but tensile radial stresses, while the yttrium region was subjected to tensile hoop stress and radial stress. The inner Y region was equitriaxial, which is why the von Mises stress was so small in the center. Also, this analysis implies that the cracks could have started anywhere in the Y region. Figure 3 shows a picture of two cracked yttrium hydride rods that were fabricated under conditions that rapidly

supplied H into the solid, resulting in a large hydrogen concentration gradient throughout the hydrided work pieces (i.e., the H gas–solid surface flux is much larger than the H diffusive flux in the solid).

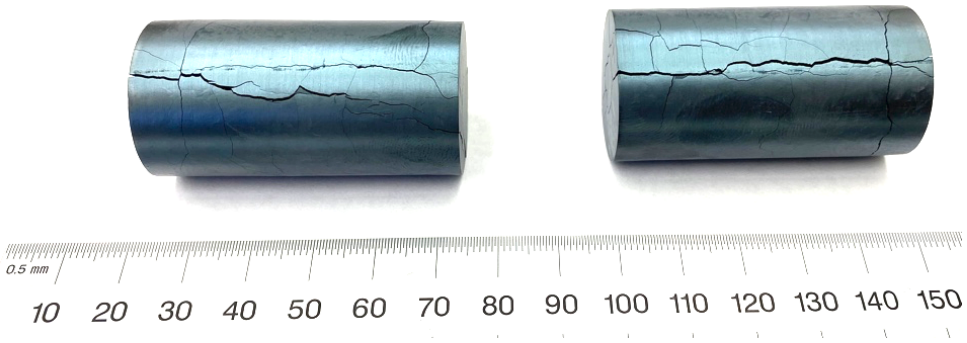

Figure 3. Cracked yttrium hydride rods resulting from the presence of the large hydrogen concentration gradients within the samples during fabrication [23].

The fourth simulation considered a case with a shallow H concentration gradient in which the center was $YH_{1.74}$ and the surface was $YH_{1.84}$. This represents a scenario in which H was slowly supplied to the solid, so there was ample time for diffusive flux to flatten the H concentration profile inside the solid. This simulation predicted much smaller stresses. Therefore, crack prevention appears to be clearly a matter of preventing large concentration gradients within the sample. A practical approach is to initiate hydriding at the desired final temperature but to limit the rate of hydriding at said temperature by applying a small hydrogen flow rate to allow more time for hydrogen redistribution (via bulk diffusion process) within the workpiece, thus avoiding an adverse hydrogen concentration gradient in the sample. Uniformity of retort temperature is generally of primary importance in producing sound massive metal hydrides with uniform hydrogen/metal atom ratios.

2.2 Fabrication of bulk crack-free yttrium hydride

A fully programmable hydriding system with continuous hydrogen partial pressure and flow control coordinated with precise temperature control has been designed and constructed at ORNL to fabricate yttrium hydride. A schematic plot of this system is shown in Figure 4: an ultra-high vacuum system consisting of all metal parts and fittings capable of a vacuum level of 2×10^{-8} torr. The maximum temperature of the 3-zone tube furnace is 1,100°C. An Inconel retort is employed to process the sample. The programmable gas control system was designed to enable flow control coordinated with temperature control. An automatic emergency cut-off system with a safety inert gas purge line and a pressure relief valve was included to ensure safe hydrogen handling.

Instead of introducing a set amount of hydrogen to the retort, yttrium hydride is fabricated by carefully matching the retort temperature and the hydrogen partial pressure. The process was initiated with ultra–high-purity yttrium metal—99.99%, purchased from American Elements—to avoid the effects of impurities. The typical hydriding process is designed as follows:

1. Evacuate the retort after loading yttrium samples and run Ar purges;
2. Heat the retort to 900°C to degas under vacuum, and then lower the retort temperature to the pre-determined processing temperature;
3. Isolate the retort from the pumping system using the gate valve;
4. Introduce ultra–high-purity hydrogen to the retort at a low flow rate ranging from 5 to 150 sccm, depending on the surface area of the material to be hydrided;

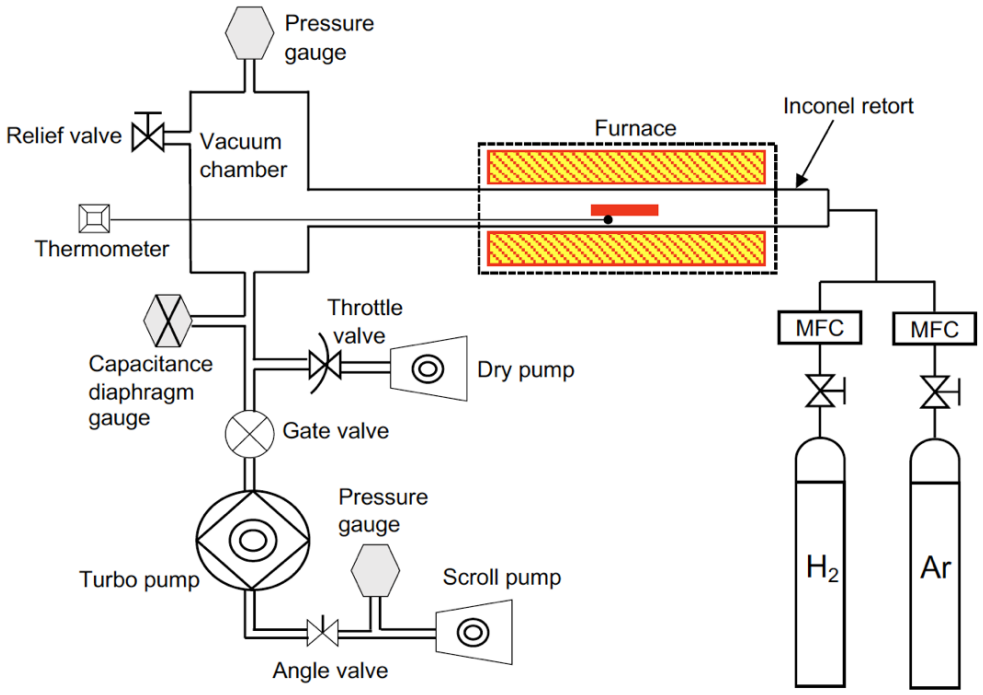

Figure 4. Schematic of the TCR bulk metal hydriding system at ORNL [23].

5. Maintain the hydrogen pressure within the retort to a predetermined value that, together with the processing temperature, determines the H/Y atomic ratio of the final product, and maintain a close coordination of the throttle valve, the mass flow controller, and the capacitance diaphragm gauge to yield the constant retort pressure;
6. Bring the retort to room temperature following the temperature-pressure isochore line. Precise pressure control corresponding to the retort temperature is achieved using the same instruments during this step.

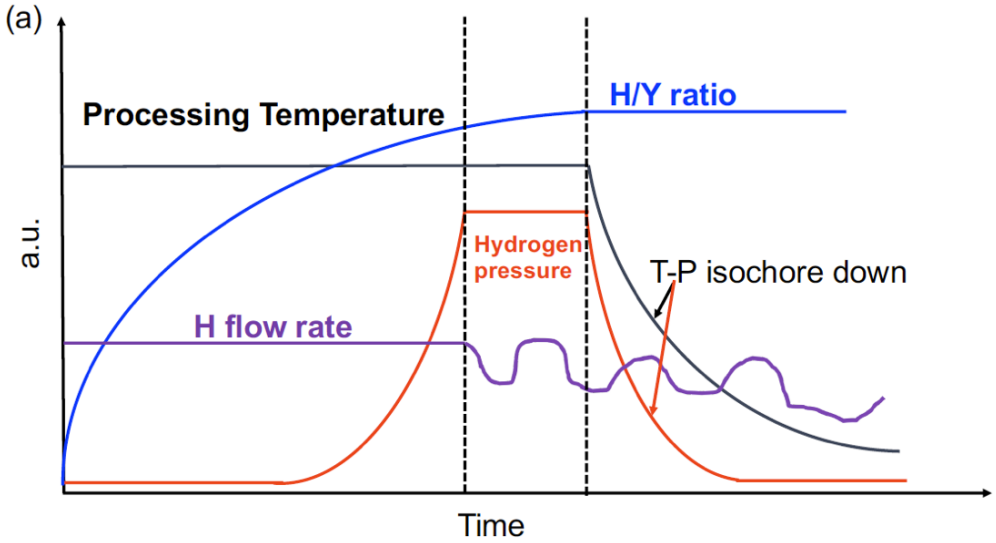

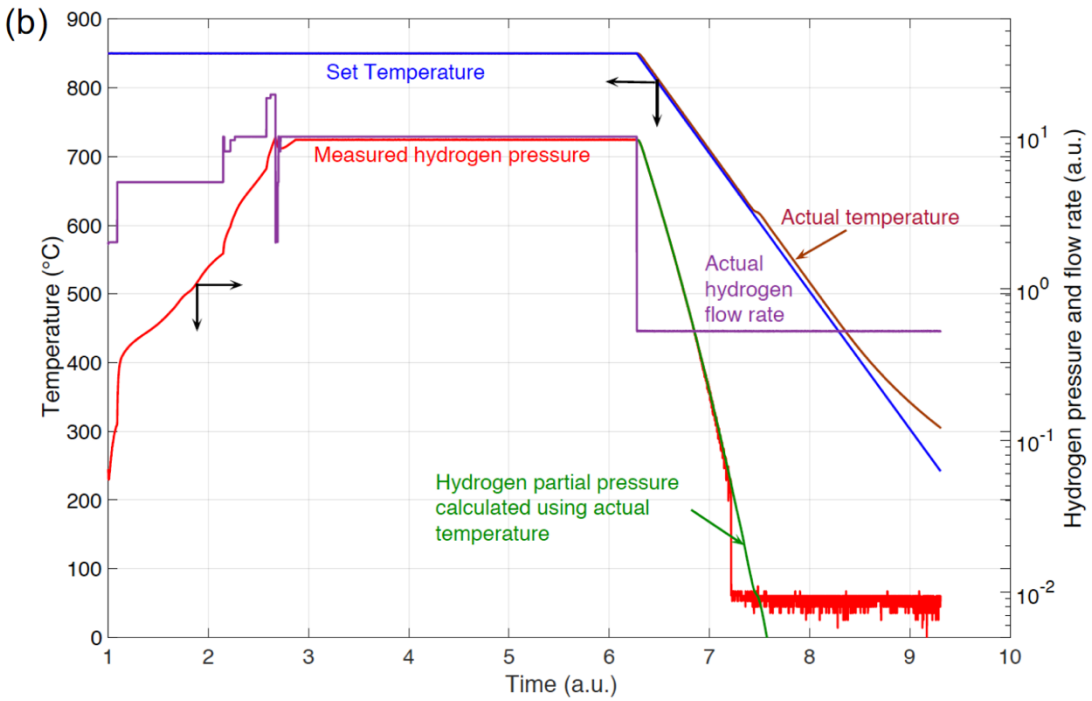

Figure 5. (a) Schematic plot of the evolution of retort temperature, hydrogen partial pressure, hydrogen flow rate, and H/Y atomic ratio during a desired hydriding process, and (b) the important processing parameters recorded during a typical hydriding process. The theoretical hydrogen partial pressure calculated using the recorded temperature is also shown (bright green line) [23].

The evolution of important parameters during the hydriding process is schematically shown in Figure 5(a). A constant hydrogen flow rate is initially maintained to provide hydrogen supply to the retort. The work piece rapidly absorbs the introduced hydrogen, resulting in a stable vacuum environment in the retort. Then the hydrogen pressure in the retort begins to increase slowly, indicating the onset of hydride formation. Eventually, the hydrogen pressure reaches a threshold that is predetermined based on the desired H/Y atomic ratio in the final product and the processing temperature. Then the hydrogen's partial pressure in the retort will remain constant to enable homogeneous distribution of the hydrogen across the sample. During the cooling down process, the temperature-pressure isochore line must be followed to maintain the H/Y atomic ratio in the final product, which requires the simultaneous controls of temperature and hydrogen partial pressure. An *isochore* is a line of constant composition on a plot of temperature vs. pressure, which has been well established through thermodynamics studies [24]. By following the isochore line, it is possible to maintain the hydrogen concentration of fabricated yttrium hydride without either absorbing hydrogen from or evolving it to the surrounding atmosphere during the furnace cooling process. Figure 5(b) shows the hydrogen partial pressure, the hydrogen flow rate, and the temperatures recorded during a typical hydriding process. The theoretical hydrogen partial pressure calculated using the recorded temperature and the correlation of temperature and hydrogen pressure with respect to a specific H/Y atomic ratio from Ref. [24] was also shown to exhibit the excellent control of the system's hydrogen partial pressure.

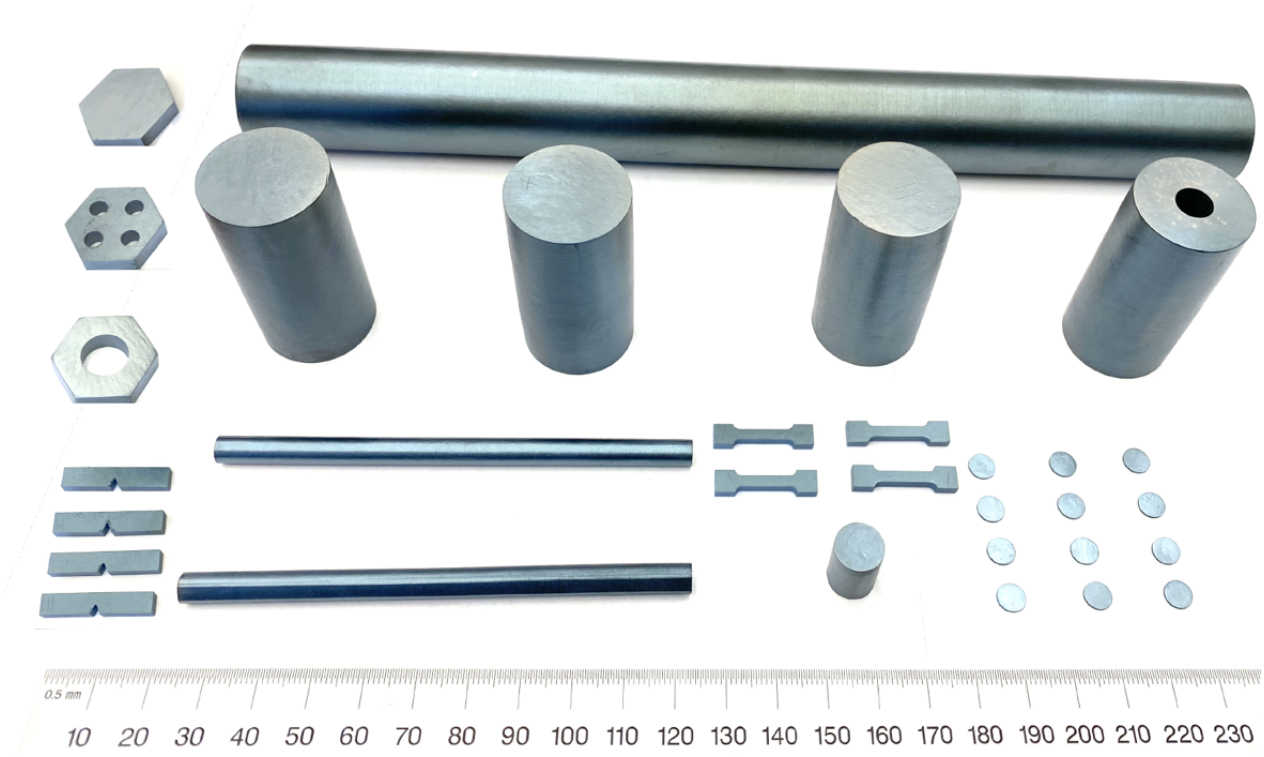

Figure 6. Yttrium hydride samples with various geometries fabricated using the ORNL hydriding system [23].

2.3 CHRACTERIZATION OF FABRICATED YHX

Following the fabrication procedure outlined above, crack-free YH_x disks, pellets, rods, bars, tensile test specimens, and hexagonal coupons with complicated geometries were successfully fabricated at ORNL, as shown in Figure 6. Optical microscopy observation showed that there is no visible cracking on the as-fabricated yttrium hydrides and only the pattern following surface polishing of the starting yttrium metal is observed, as shown in Fig. 7. The H/Y ratios of the yttrium hydride samples (0.1 ~ 600g) shown in Figure 6 range from 1.65 to 1.90. The hydrogen concentration in the hydrides was determined based on the weight change before and after the hydriding process. The large weight gain in the large-scale samples (e.g., >2% weight increase resulting from hydrogen absorption during the hydriding process) allows the hydrogen concentration in the fabricated hydrides to be more accurately determined. The hydrogen concentration was also measured using the hot vacuum extraction technique (Luvak Inc.) to assess the accuracy of the hydrogen concentration as determined by weight change. The results are shown in Table 1. The H/Y atom ratios determined by the weight change method and the vacuum hot extraction technique are comparable, within 4% uncertainty, except in YHR-3. Therefore, the method for determining the H/Y atomic ratio according to weight change will be used in the R&D of yttrium hydride.

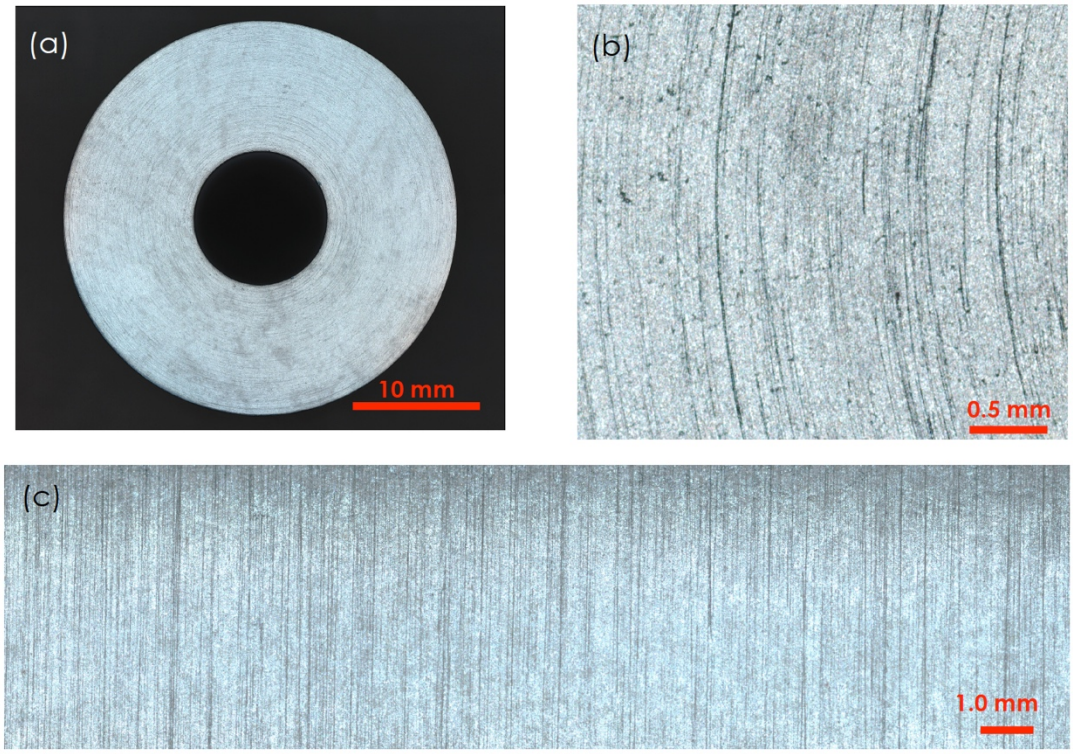

Figure 7. Optical microscopy of the (a-b) end surface and (c) side surface of an as-fabricated yttrium hydride annular rod [23].

XRD analysis was used to confirm the phases present in the fabricated hydride samples. XRD samples were prepared by depositing YH_x powder on a zero-background (for 2θ<120°) silicon dioxide single-crystal sample holder. Samples were also mixed with lanthanum hexaboride (LaB6) powder (NIST SRM660b), which served as an internal standard during pattern refinement. XRD diffraction patterns were obtained using a Bruker D2 Phaser benchtop x-ray diffractometer of 0.30 kW with Cu Kα radiation. Rietveld refinement was performed on the experimental patterns using the General Structure Analysis System [33]. A typical powder XRD pattern of a fabricated $YH_{1.88}$ is shown in Figure 8. Based on the analysis, it is apparent that both the δ-phase yttrium hydride and the α-phase metal yttrium are present in the fabricated hydride material. The XRD results from selected yttrium samples are summarized in Table 1. The fraction of δ-phase yttrium hydride is a function of the H/Y ratio, and it increases with the increasing H/Y ratio. The absence of any noticeable oxide phase underlines the well-controlled vacuum environment within the system, implying that the H/Y atomic ratio as determined by weight change during the hydriding process is reliable.

Table 1. XRD results of as-fabricated YHx pellets.

Sample	H/Y ratio		XRD	
	Weight change method	Hot vacuum extraction	δ-phase YH_2 (wt%)	α-phase Y (wt%)
YHR-1	1.70	1.72	81	19
YHR-2	1.52	1.57	77	23
YHR-3	1.59	1.71	72	28
YHR-4	1.84	1.89	>99	<1
YHR-5	1.88	1.87	>99	<1

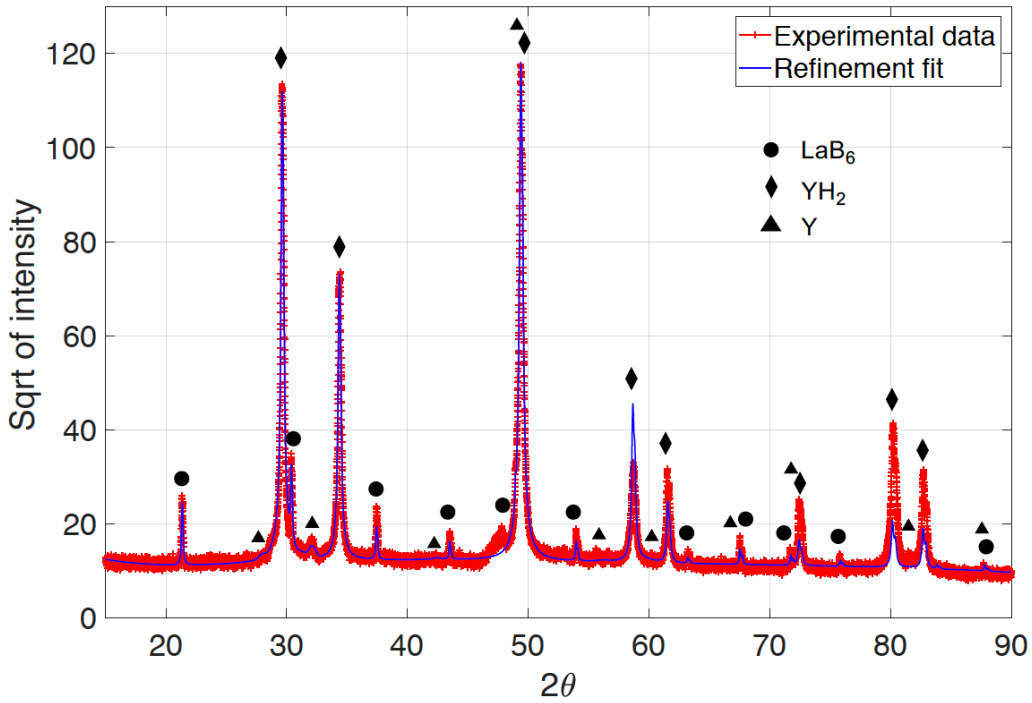

Figure 8. XRD pattern of $YH_{1.88}$ along with Rietveld refinement fit [23].

TCR program has successfully demonstrated the fabrication of bulk crack-free yttrium hydride in FY2020. The hydriding process and the characterization of the as-fabricated hydride have been published in the Journal of Nuclear Materials [23]. With bulk crack-free yttrium hydride now available, a comprehensive R&D campaign was initiated under the TCR program at ORNL to establish a complete database summarizing the basic physical and thermomechanical properties of yttrium hydride, as well as the irradiation response needed to facilitate its deployment as a high-temperature moderator material in advanced thermal neutron spectrum reactors. In the following sections, selected thermomechanical properties are reported.

3. THERMAL PROPERTIES OF YTTRIUM HYDRIDE

The thermophysical properties of yttrium hydride have been measured in FY2020 and the results have been included in a manuscript that is under review in the Journal of Nuclear Materials. Here, we are presenting the thermal diffusivity, the specific heat capacity, the thermal conductivity, and the coefficient of thermal expansion of yttrium hydride as a function of temperature and hydrogen concentration. In addition, a reversible 2nd order transition of the measured thermophysical property was identified and the possible underlying mechanisms will be discussed.

3.1 EXPERIMENTS

3.1.1 Materials

Yttrium hydride rods (10mm in diameter, 15mm in height, approximately 5.4 g) were fabricated with H/Y atomic ratios ranging from 1.52 to 1.88. The hydrogen concentration was determined by the weight gain of the samples before and after hydriding. Fig. 9 showed a picture of five as-fabricated hydride rods. Following the characterization of the as-fabricated hydride rods, these rods were embedded inside epoxy and sectioned

into disks with approximately 1 mm thickness by using a slow speed diamond saw for further thermomechanical property measurements.

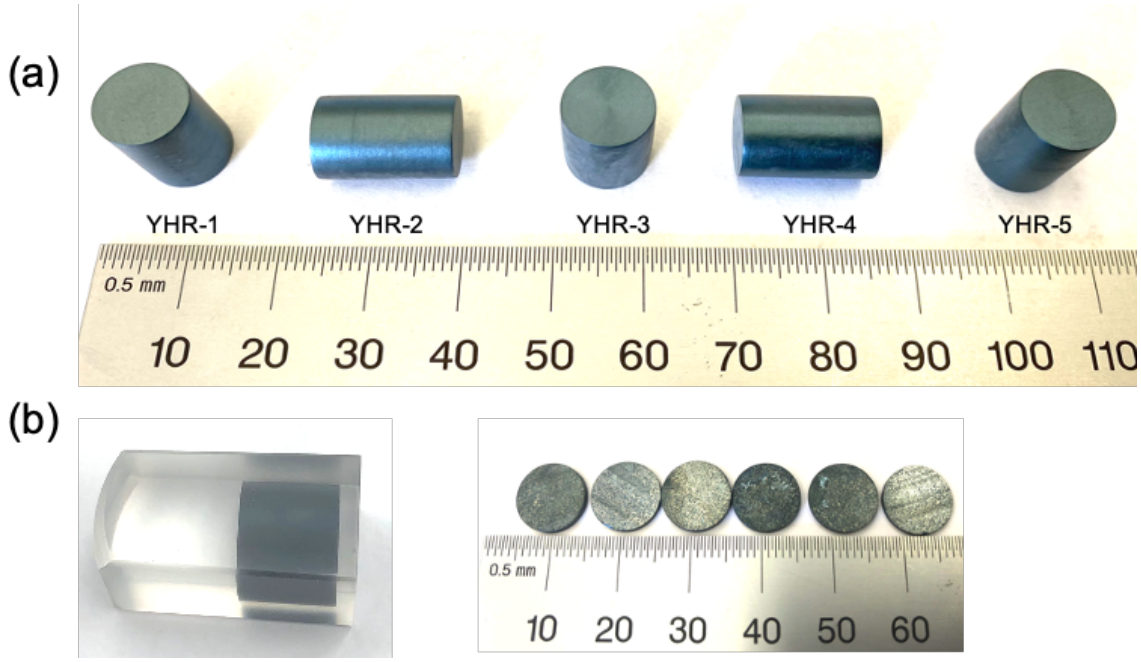

Figure 9. (a) As-fabricated yttrium hydride rods; (b) an yttrium hydride rod embedded inside epoxy and the sectioned slices.

3.1.2 Specific heat capacity

Specific heat capacity was measured according to ASTM E1269 [34] at 10°C/min using a Netzsch differential scanning calorimeter (DSC) 404C. Temperature ranged from room temperature to 500°C for YH_x, with x = 1.88 and 1.84, and from room temperature to 700°C for YH_x, with x = 1.70, 1.59, and 1.52. Each sample underwent two full heating and cooling DSC runs to confirm reproducibility. Platinum pans and lids were used during the DSC runs. Sapphire was used as a standard reference material. YH_x samples were 5.5 mm diameter disks that were 1 mm thick. Prior to the experiments, the DSC furnace was purged with argon three times. The DSC runs were conducted with flowing titanium-gettered argon, and the oxygen level was kept below 10^{-8} ppm. Upon completion of a heating cycle, samples were held at the maximum temperature for 20 minutes before starting a cooling cycle.

3.1.3 Thermal diffusivity and thermal conductivity

Thermal diffusivity measurements were performed according to ASTM E1461 [35] using a Netzsch Laser Flash Technique (LFA) 457 laser flash system. A temperature range from room temperature to 500°C was used for YH_x with x = 1.88 and 1.84 and from room temperature to 700°C for YH_x, with x = 1.70, 1.59, and 1.52. Samples were 10 mm diameter disks that were 1.5 mm thick. No coating was applied to the samples. The testing was performed under argon purge gas at 100 mL/min. The diffusivity values are calculated based on the sample thickness and the temperature rise curve after each laser pulse using the Cowan method with pulse width correction [36, 37]. Three measurements were performed at each temperature set point for every sample, and the average values with the standard deviation are reported.

Thermal conductivity (κ) was calculated after measuring thermal diffusivity (α) using the laser flash method and specific heat capacity (C_p) using the DSC. Using RT density (ρ), thermal conductivity values from

room temperature to 500°C or 700°C, depending on the composition were calculated using the following equation:

$$\kappa = \alpha \cdot \rho \cdot C_p \quad (1)$$

3.1.4 Thermal expansion

The coefficient of linear thermal expansion (CTE) was measured using a Theta Dilatronic IX differential dilatometer, which is a horizontal dual pushrod dilatometer. The YH_x samples were 6 mm diameter cylindrical rods 25 mm long with a hydrogen content of x = 1.61, 1.68, 1.75, 1.81, 1.85, 1.87, 1.93. The temperature range was from 100 to 700°C. A heating/cooling rate of 3°C/min was used. Each sample was measured twice to confirm reproducibility, and a sapphire standard was used as a reference. Before each run, the vacuum-tight dilatometer was pumped down and back-filled with helium three times, and then it was pumped down a final time to below 200 mTorr. During the run, titanium-gettered helium flowed through the system at 15 sccm.

3.2 RESULTS

3.2.1 Specific heat capacity

Figures 10a and 10b show the specific heat capacities, C_p, of five yttrium hydrides YH_x as a function of temperature T, where x = 1.88, 1.84, 1.70, 1.59, and 1.52. The results in Figure 10a show that at the lower temperatures (<300°C), the specific heat capacities for the samples with higher H/Y ratios were higher than those with lower hydrogen concentration. This is expected since more H atoms exist in the lattice per unit mass: note that if the heat capacity were normalized to J/mole-H/K, then the trend would be the opposite. The samples also showed gradual increase of C_p with the temperature until a certain value, at which point a heat capacity anomaly was observed as represented by a sharp drop, followed by the reestablished positive slope. The observed λ-type C_p is consistent with the second-order transitions similar to the Curie temperature for ferromagnetic to paramagnetic transition or order–disorder transitions [38]. The transition appeared to be reversible since the sharp increase of C_p during cooling cycles was present, as shown in Figure 10b. The transition temperature was lower for the samples with higher H/Y ratios, and its values appeared to be lower during the cooling cycles than during the heating cycles. The observed difference between heating and cooling can be partially attributed to the thermal lag between the measured temperature and the actual temperature of the samples. The second DSC run of each sample confirmed the repeatability and reversibility of the transition. Another noticeable feature of the specific heat capacity was that following the transition, the dependence of the H/Y ratio on the specific heat capacity was negligible within instrument uncertainties of ±2–3%, as manifested by the observation that all measured curves fall onto the same line. Figures 10c and 10d display the baseline-corrected DSC curves and their first derivatives, respectively, of $YH_{1.59}$ sample, as a representative example. The curves are matched against the measurement of the sapphire standard reference material (SRM) to emphasize the region where the change in the heat flow occurs corresponding to the transition in the heat capacity plots and to indicate the endothermic nature of the discussed transition upon heating and the exothermic transition upon cooling.

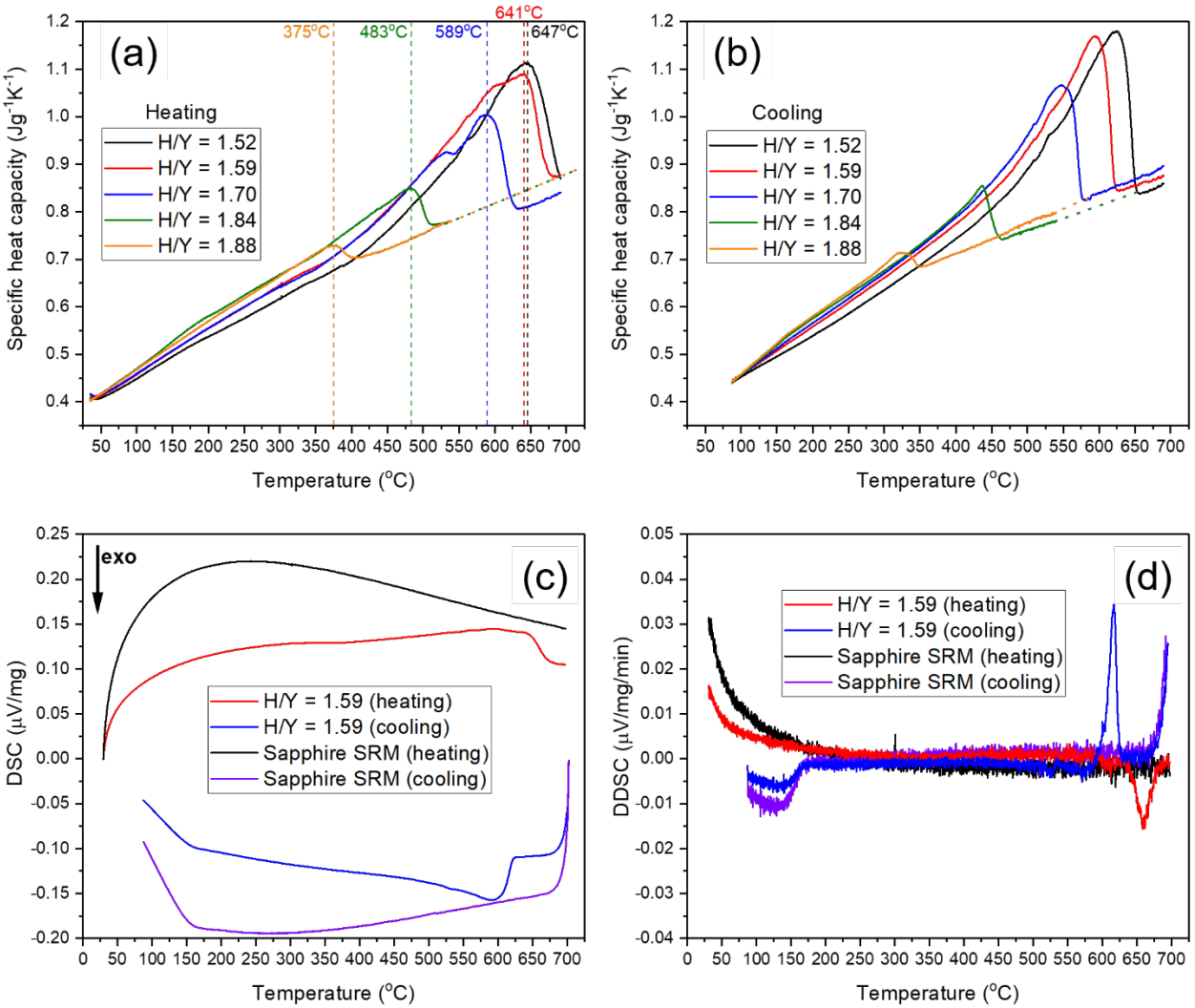

Figure 10. (a–b) Specific heat capacity C_p of YH_x as a function of temperature for various H/Y ratios. (a) Heating cycle; (b) Cooling cycle (dotted lines are extrapolations of $C_p(T)$ to highlight similar heat capacity after the transition for all the samples); (c) DSC curves; and (d) their first derivatives as a function of temperature for the $YH_{1.59}$ sample and a sapphire SRM.

3.2.2 Thermal diffusivity

Figure 11a shows the thermal diffusivity, α, of yttrium hydrides with the same H/Y ratios used to obtain the heat capacity. In general, the thermal diffusivity was higher for the samples with larger H/Y values, and it decreased as a function of temperature, showing typical phonon scattering due to the changes in the mean free path. When the data were taken at 50–100°C steps, the results were similar to those found in the literature [39]. However, when the diffusivity data were taken at 5–10°C steps before and after the expected transition temperature, a clear change in the slope was observed that can be correlated with the discussed shift of heat capacity. This change was subtle and would be difficult to recognize without corresponding C_p data and small temperature increments. As shown in Figure 11b, the transition temperatures seen in the thermal diffusivity experiments match those from the specific heat capacity plots. Figure 11b only shows overlaps of the results for the samples with the lowest and the highest H/Y ratios, but the same applies for all the compositions.

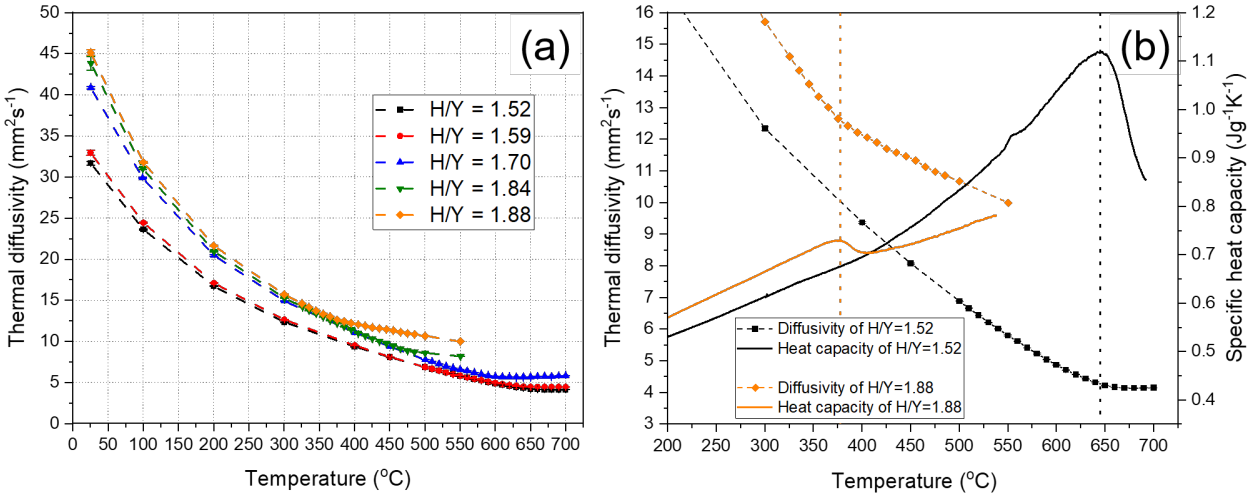

Figure 11. (a) Thermal diffusivity of YH_x as a function of temperature for various H/Y ratios (heating cycle). (b) Overlap of thermal diffusivity and specific heat capacity as a function of temperature for the lowest and the highest H/Y ratios emphasizing similar transition temperatures. Dashed lines serve only as guides for the eye.

3.2.3 Thermal conductivity

The thermal conductivity κ, shown in Figure 12, was derived from the specific heat capacity, the thermal diffusivity, and the density according to Eq. (1). RT density was used, with its values being 4.264 for $YH_{1.88}$, 4.252 for $YH_{1.84}$, 4.271 for $YH_{1.70}$, 4.274 for $YH_{1.59}$, and 4.280 g/cm^3 for $YH_{1.52}$. As in the diffusivity results, the κ decreased with temperature, being higher for larger H/Y ratios, and becoming more similar at higher temperatures. Change of the slope at higher T, as observed in Figure 12, was expected since the thermal conductivity was estimated from aforementioned C_p and α, and the values after the transition followed a less steep slope, indicating that the high temperature phase may have less defects for phonons scattering. The thermal conductivity results were close to those reported in the literature on YH_x with the similar compositions [39]; however, there was no report of the changes in the material's response at high temperatures. Upon close inspection of the results for $YH_{1.90}$ from the 2005 publication by Ito et al. [39], the deviation of thermal diffusivity and thermal conductivity trends from the other two YH_x samples can be recognized at around 625 K (350°C). According to the inverse proportionality of the transition temperature to the hydrogen content established in the present work, the noted temperature would be in agreement with a transition temperature of approximately 372°C of the $YH_{1.88}$ sample from Figures 11 and 12. Furthermore, onset of the transition for $YH_{1.86}$ and $YH_{1.72}$ from the 2005 publication by Ito et al. [39] would be expected at around or above 700 K (427°C), at which point only two and one data points, respectively, were reported, making it difficult to judge a potential change in the response. No such change could be seen in the heat capacity and thermal conductivity shown in the work by Ito et al. [39], which could be due to large temperature increments of the measurements.

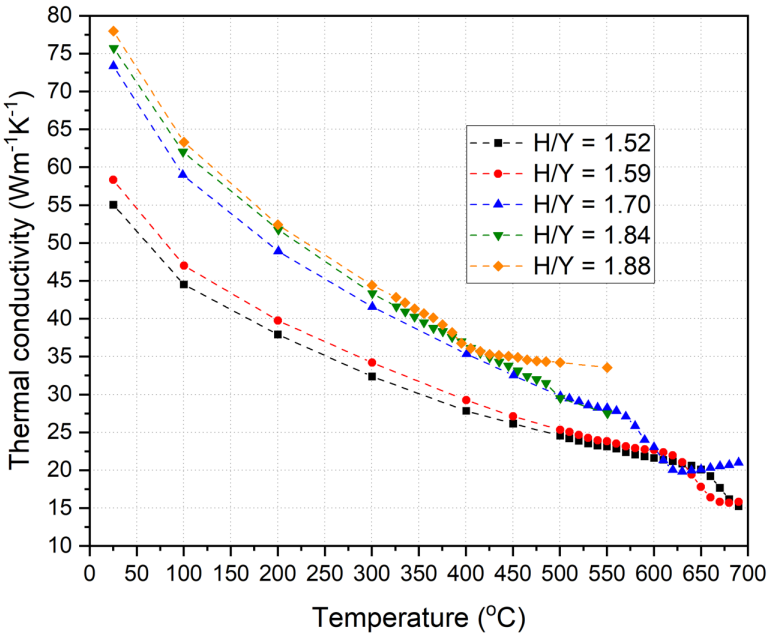

Figure 12. Thermal conductivity of YH_x as a function of temperature for various H/Y ratios calculated using measured thermal diffusivity, specific heat capacity, and RT density according to Eq. (1). Dashed lines only serve as guides for the eye.

3.2.4 Coefficient of thermal expansion

The changes in the CTE with the temperatures are shown in Figure 13. CTE continuously increased as a function of temperature in all samples, and it eventually changed the slope past the transition temperature, similar to the behavior seen with the other thermal properties. The higher hydrogen concentration in the samples resulted in the lower CTE past the transition temperature. It is known that the transition from α-phase yttrium to δ-phase yttrium hydride leads to up to 6% volume expansion [40]. It is noted that more α-phase yttrium is present in YH_x with a lower H/Y atomic ratio. Therefore, it is expected that dimensional change in YH_x with lower H content is more significant. The exception in this work was the $YH_{1.93}$ sample, which was a single-phase hydride. $YH_{1.93}$ showed the lowest CTE values with the smoother change as a function of temperature relative to the samples with lower H/Y ratio and in the absence of observable transition. The linear thermal expansion coefficient of δ-phase yttrium hydride was reported to range from 7.5×10^{-6} to 13×10^{-6}/K in the temperature regime of 100–627°C [41], which is consistent with the results in this work.

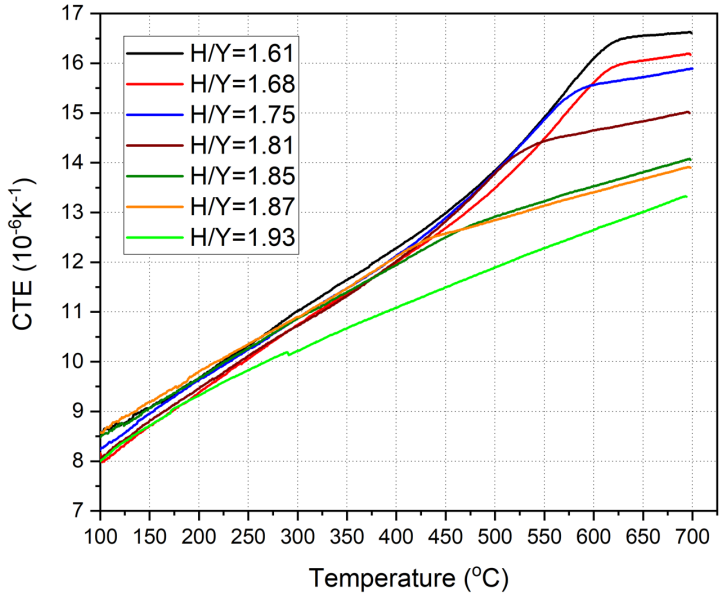

Figure 13. CTE of YH_x as a function of temperature for various H/Y ratios (heating cycle).

The transition temperatures as a function of hydrogen content were determined from the results of heat capacity, thermal diffusivity, and CTE, as displayed in Figure 14. The dependence was nonlinear and inversely proportional to H/Y, but it showed an agreement between the values derived from the different thermophysical properties. The extracted data points were fitted with the exponential decay function shown in Figure 14 to help guide the eye.

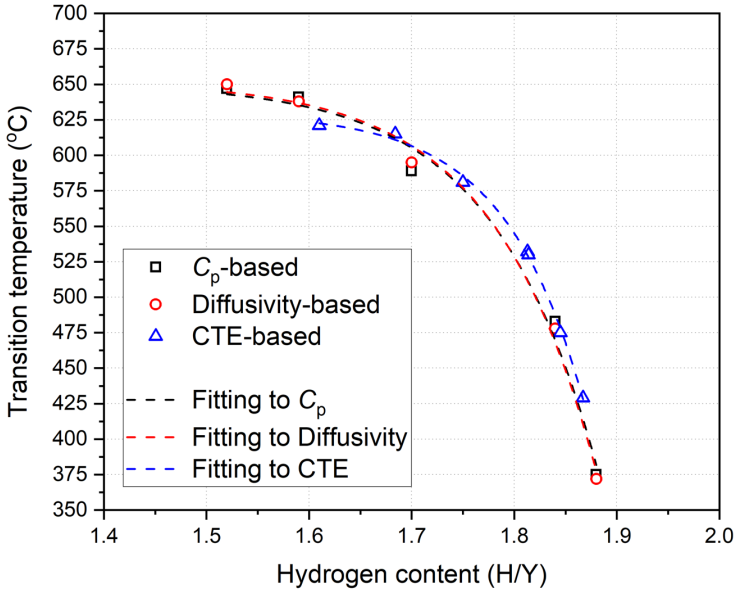

Figure 14. Transition temperature as a function of the H/Y ratio estimated from the specific heat capacity (C_p), the thermal diffusivity, and the CTE data. Symbols are experimental values; dashed lines are corresponding fitting curves to guide the eye.

3.3 DISCUSSION

As shown in Section 3.2.1, the specific heat capacity data clearly indicate that a reversible second-order endothermic phase transition occurred in the high-temperature regime, and the transition temperature was

a function of the H/Y ratio in the investigated materials. To address the nature of the identified changes in the material properties with temperature and hydrogen concentration, the nonstoichiometry in yttrium hydride phase must be considered. As shown in Figure 15, hydrogen exhibits ample solubility in α-Y metal, and some of this saturated metal phase remains in the samples of lower H/Y ratio studied in this work. Upon increase of H/Y ratio, single δ-YH_x is formed, and further increase of the hydrogen content leads to a formation of trihydride, which is beyond the H/Y values considered here. The two condensed phases, α-Y and δ-YH_x exist in equilibrium as shown in the two-phase region of Figure 15, where the H/Y ratio in each phase is fixed by the phase boundaries at any given temperature. Based on the phase diagram, the H solubility in the δ-YH_x, which is in equilibrium with α-Y, decreases with increasing temperatures, while the H solubility in α-Y increases. Upon heating of the current samples, the total H/Y ratio for the closed system is fixed, but the H is released from δ-YH_x and transferred to α-Y, allowing transformation from α-Y to δ-YH_x. Figure 15 displays an overlap of the transition temperatures extracted from the current C_p and CTE experiments, including both heating and cooling cycles, with the calculated phase diagram of Y–H binary system and reported experimental phase equilibrium data [24, 26, 42-49]. The experimentally determined transition temperatures are higher than the predicted phase boundary, indicating that an additional process might be involved in the changes of thermal properties.

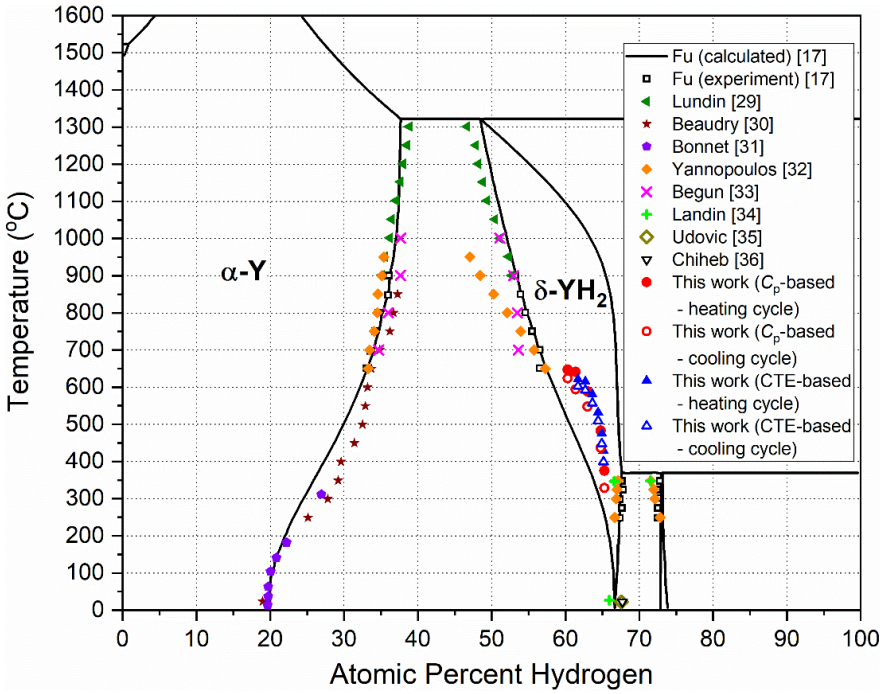

Figure 15. Y-H binary phase diagram summarizing the data available in the literature [24, 26, 42-49] and the data from the present work.

α-Y to δ-YH_x transformation cannot fully explain the observed λ-type peak in the heat capacity curves since the discussed phase transformation is a first-order transition, while the features seen in the Figure 10a suggest a second-order transition in the investigated samples. By using the Gibbs energy functions reported in Fu et al. [26], the enthalpy change for the same H/Y ratios as a function of temperature was calculated as shown in Figure 16. A kink is observed in each curve, suggesting the transition from the (α-Y + δ-YH_x) two-phase region to the δ-YH_x single-phase region. The transition temperature increased as H/Y ratio decreased, which is consistent with the calculated phase diagram in Figure 15. The convex kink indicates that the nature of the transition is exothermic, which is opposite to the endothermic transition observed in heating cycle of the DSC experiments (Figures 10d). Therefore, the phase transformation from the α-Y to

the δ-YH_x phase is not the main contributor to the λ-type peak in the specific heat capacity plots shown in Figure 10a.

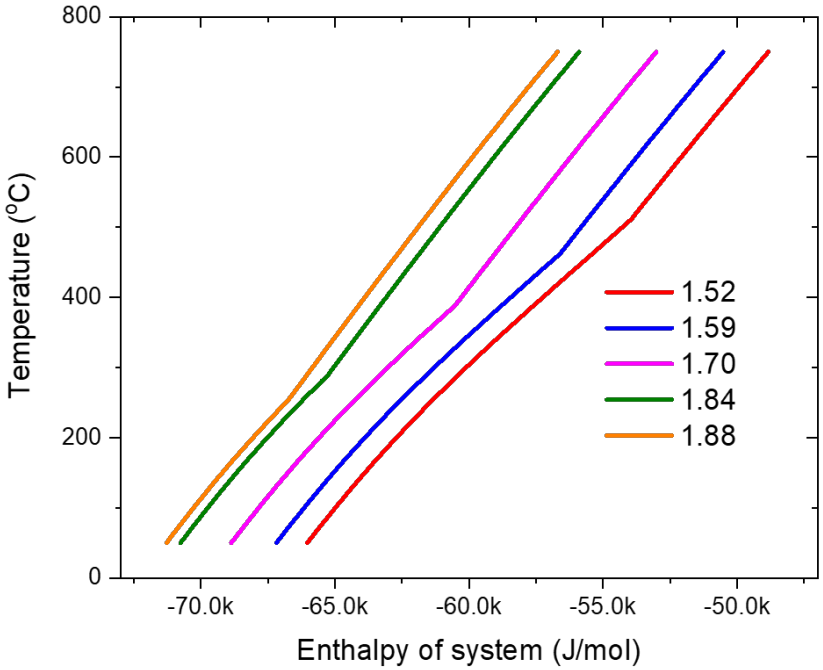

Figure 16. Enthalpy change for YH_x as a function of temperature calculated based on Gibbs energy functions reported in Fu et al. [26].

Alternatively, the reversible second-order phase transition in metal hydride could be induced by the hydrogen order–disorder rearrangement. For example, the endothermic lambda-shape peaks in the heat capacity curves of hafnium hydrides measured with the DSC were attributed to the δ'/δ phase transition correlated to the redistribution of hydrogen [50]. In the δ-YH_x, while it is expected to have a fluorite structure—in which the yttrium atoms create a FCC and the hydrogen atoms occupy the tetrahedral (T) positions [51]—multiple techniques (neutron diffraction, nuclear magnetic resonance, optical spectroscopy) applied to the selected δ-YH_x revealed a deviation from the purely tetrahedral structure due to filling of octahedral (O) sites in FCC before all of the T-sites (energetically preferred) were occupied [52-55]. The fraction of O-sites occupied in δ-YH_x is defined as the intrinsic disorder, and the experiments using a variety of spectroscopic techniques have verified appreciable (~10%) intrinsic disorder at RT. Although the correlation between the temperature and the fraction of hydrogen atoms in O-sites is still unclear, as controversary conclusions were observed from a number of studies ([55, 56] and the references therein), it is possible that the prevailing process of the second-order transition presented in Figure 9 arises from the lattice disorder caused by the hydrogen occupation of O-sites at the expense of T-sites and the consequential redistribution of hydrogen.

Given this information, it is evident that the thermal property measurement process simultaneously involves the α-δ phase transition and the order–disorder transition. The latter continues following the completion of the α-δ phase transition and it dominates the observed λ-shape peaks in the specific heat capacity curves. Therefore, the transition temperatures determined from the measurements of the thermal properties are expected to be higher than those determined from the phase diagram, as was observed in Figure 15. However, a robust conclusion cannot be obtained based on the comparison of these values due to the experimental uncertainties. Performance of additional characterization, such as high-temperature neutron scattering or high-temperature XRD, could elucidate the hydrogen occupancy in YH_x as a function of temperature and H/Y ratio; these tasks have been included in the work scope of the TCR program.

4. MECHANICAL PROPERTIES OF YTTRIUM HYDRIDE

4.1 VICKERS HARDNESS

Vickers hardness measurement was carried out on the yttrium hydride disks (1mm in thickness, 10mm in diameter, Section 3.1.1) using Buhler Tukon3100. The applied load and the dwell time for the indentation are 200g and 15 s, respectively. 10 measurements were performed on each sample to obtain good statistics. The values of the Vickers hardness obtained for YH_x are shown in Fig. 17 as well as the available literature data. The results showed that higher hydrogen concentration results in larger hardness within a relatively narrow regime of 1.8~2.5 GPa. Setoyama's hardness values [20] are higher than the presented values and scattering within a large range of 3~4.5GPa. In addition, the hardness reported in Ref. [57] fell onto the trajectory of our hardness data.

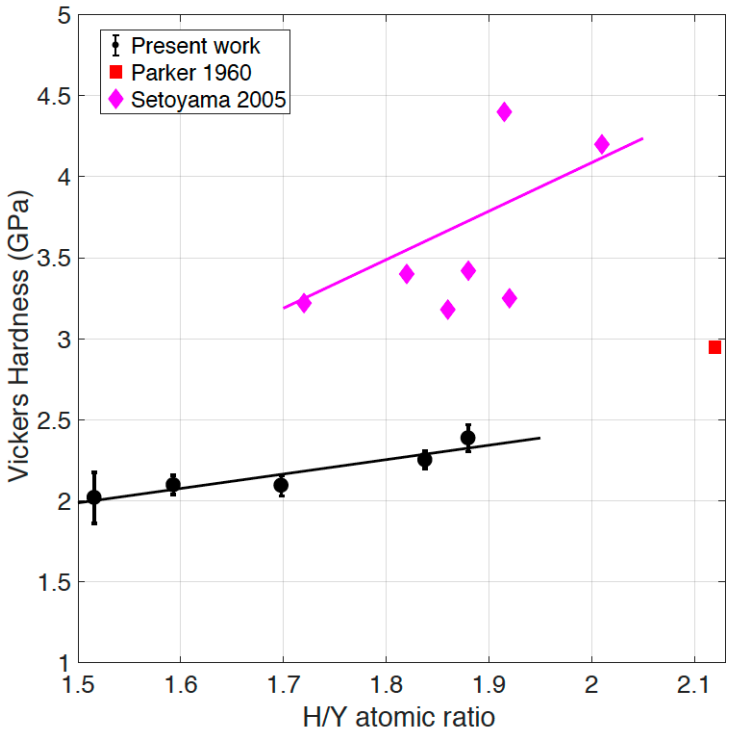

Figure 17. Vickers hardness of yttrium hydride as a function of H/Y atomic ratio.

4.2 NANOINDENTATION

Nanoindentation mapping has been used in this work as a means to investigate the correlation of mechanical properties, specifically Young's modulus and hardness, with crystal orientation using combined EBSD, modulus and hardness maps. YHx disks (6 mm in diameter and1mm in thickness) were tested. A G-200 Keysight Technologies nanoindenter was used for room temperature measurements and a KLA-Tencor InSEM ® HT nanomechanical tester was used for ultra-fast mechanical properties mapping. The maps were obtained by using a high-speed nanoindentation mechanical property mapping techniques called "NanoBlitz 3D" capable of performing individual indent within a 1 second; thus, revealing high resolution and absolute maps of Young's modulus, hardness in a reasonable time of experiment. We performed 90×90 indents with the depth of 150 nm and 2.5 μm distance between two consequent indents in two and half hours. At this depth of indents, the Indentation Size Effect, which artificially induced by shallow indentation can be discarded [58].

The grid of indentation area was consequently identified by SEM imaging as seen in Fig. 18(a). The indent spacing is kept short and was intentionally set shorter than that recommended by ASTM E2546-15 [59]. This was carefully chosen balance between the requirement of a high spatial resolution and being able to measure stiffness with sufficient precision [60].

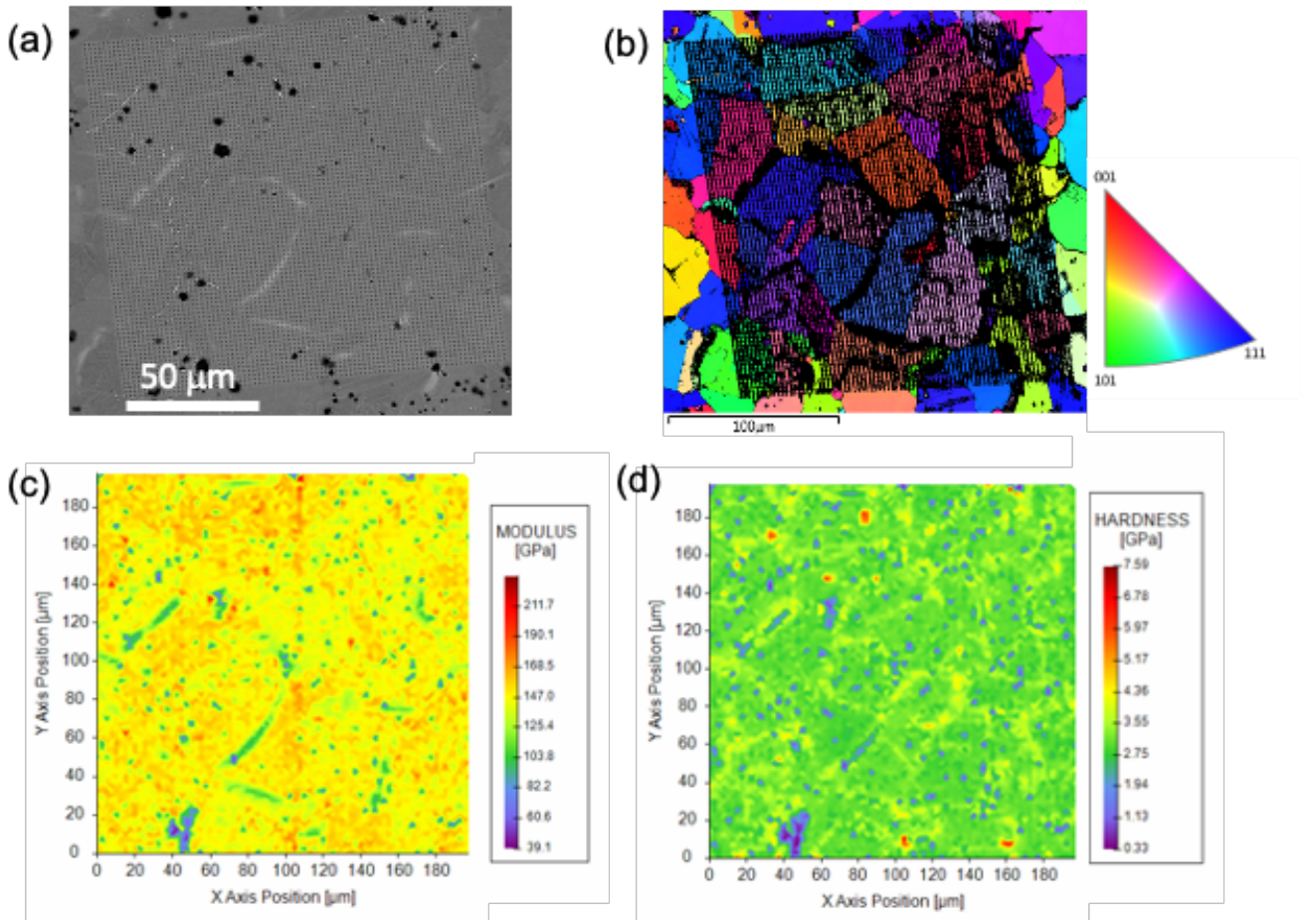

Figure 18. (a) SEM image of indentation grid, (b) EBSD, (c) Young's modulus map, and (d) hardness map of a $YH_{1.7}$ sample.

EBSD image was then obtained covering the indentation grid to reveal the correlation maps between the mechanical properties to orientation and phases, Fig. 18(b). The Young's modulus maps suggest the values slightly depend on the orientation of the hydride. The largest modulus values of 160 GPa were measured for the (111) orientation and the lowest, about 150 GPa, with the (001) orientation. The unidentified region EBSD (dark region and lines) are likely metal hydrogen solid solution that are frequently decorated along the grain boundaries showing lower modulus and hardness values. No detectable orientation dependence of hardness was found.

The dependence of Young's modulus and hardness on H/Y atomic ratio is shown in Fig. 19. The results are in agreement with previous work reported in the literature [20]. The elastic modulus of yttrium hydride in σ-YH_2 is nearly constant with H/Y ratio while its hardness slightly increased with hydrogen content. They both are substantially higher than yttrium metal (for pure metal ~65 and 0.9 GPa, respectively). The

hardness varied in the range of 2.3~3.4GPa, comparable to the values determined from Vickers hardness testing (1.8~2.5GPa.)

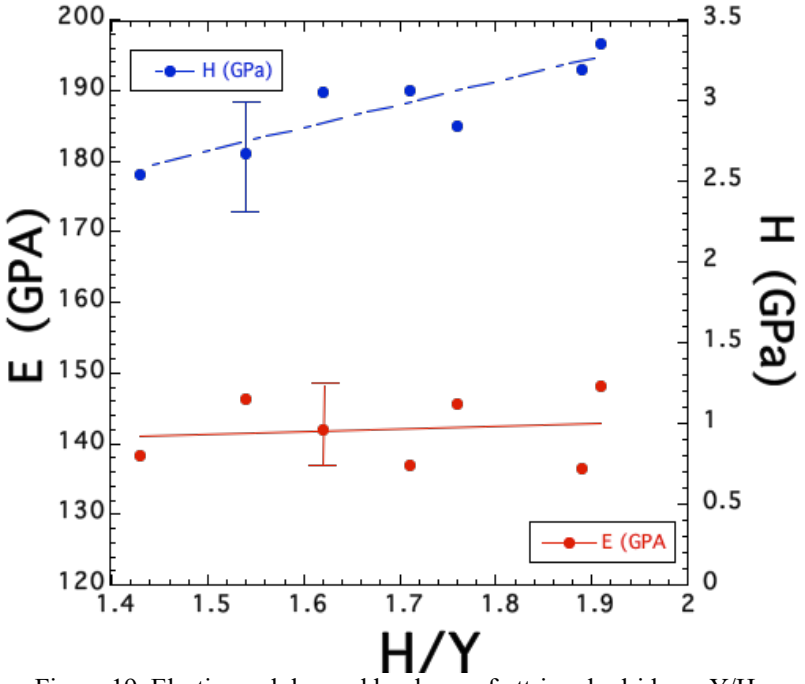

Figure 19. Elastic modulus and hardness of yttrium hydride on Y/H

5. RADIATION EFFECT STUDIES UNDERWAY

Twelve rabbit capsules containing 192 YH_x disks (6 mm in diameter, 0.5mm in thickness) have been irradiated in the high flux isotope reactor flux trap during cycle 487 (May 2020) and cycle 488 (June 2020). This irradiation test series targets temperatures of 600°C and 900°C and three different doses, 0.1, 1 and 2 dpa, which correspond to approximately 0.05, 0.5 and 1 irradiation cycle. The capsules contain disk specimens with a hydrogen concentration of either $YH_{1.72}$ or $YH_{1.87}$. The disk specimens are 0.5 mm thick and have a diameter of 6 mm. The irradiation test matrix is presented in Table 2. More information regarding the irradiation capsule design is available in the report of ORNL/TM-2019/1310.

All YH_x capsules have been shipped to hot cell for disassembly. TMs and specimens will be shipped to LAMDA for PIE. PIE will focus on assessing the thermophysical and thermomechanical properties of YH_x such as swelling, density, thermal diffusivity, specific heat, Vickers hardness, flexural strength. Microstructure and metallography (optical microscopy) analyses will also be performed. Density measurements will be performed using the helium pycnometry technique. Finally, the average irradiation temperature of each capsule will be determined using the dilatometry method on TM specimens in each rabbit. The PIE results are expected during the Fall 2020. The data collected will be compared with those collected pre-irradiation to assess the YH_x material behavior under irradiation.

Table 2. Yttrium hydride irradiation test matrix

Capsule ID	Irradiation Temperature	Dose (dpa)	Material
YHXT01	600°C	0.1	$YH_{1.72}$
YHXT02		1	
YHXT03		2	
YHXT04	900°C	0.1	

YHXT05		1	
YHXT06		2	
YHXT07	600°C	0.1	$YH_{1.87}$
YHXT08		1	
YHXT09		2	
YHXT10	900°C	0.1	
YHXT11		1	
YHXT12		2	

6. SUMMARY

In this report, we summarized the R&D activities of yttrium hydride moderator of TCR in FY2020, including the fabrication of bulk crack-free hydride, the thermomechanical properties and the ongoing neutron irradiation campaign.

- The challenges associated with fabricating large scale crack-free yttrium hydride were discussed as well as their mitigation strategies. The ORNL hydriding system—which is fully programmable and capable of continuous hydrogen partial pressure and flow control coordinated with precise temperature control—is introduced herein. Successful and repeatable fabrication of crack-free yttrium hydride in complex geometries and various dimensions at any desired H/Y ratio is demonstrated. Hydrogen content in as-fabricated hydride was determined by the weight change, a method that is considered reliable and which is attributed to the use of ultra–high-purity yttrium, the absence of oxide phases, and the large weight gain.
- Thermophysical properties of obtained materials were investigated as a function of temperature and hydrogen concentration. Measured specific heat capacity, thermal diffusivity, and calculated thermal conductivity all showed similar dependence at lower temperatures (<300°C), with the values being slightly higher for the larger H/Y ratios, whereas thermal expansion had a negligible composition dependence in the low temperature regime. The higher temperature data revealed a change in the material's response in relation to all investigated properties. The observed reversible transitions had a second-order and endothermic nature, and the transition temperature was inversely proportional to the hydrogen content. It was found that this transition cannot be rationalized by considering only the phase transformation from the mixed state (α-Y + δ-YH_x) to the pure δ-YH_x state. The order–disorder transition due to the relocation of hydrogen is deduced to contribute to the observed second-order endothermic transition.
- Vickers hardness exhibited an approximately linear dependence on the hydrogen concentration (H/Y atomic ratio). Nanoindentation was performed to reveal the hydrogen concentration and grain orientation dependence of elastic modulus and hardness. The results showed that the Young's modulus slightly depends on the orientation of the hydride. The largest modulus values of about 160 GPa were measured for the (111) orientation and the lowest, about 150 GPa, with the (001) orientation. No obvious orientation dependence was found for hardness.

7. REFERENCES

1. Mueller, W.M., J.P. Blackledge, and G.G. Libowitz, *Metal Hydrides.* Academic Press New York and London, 1968.
2. Edwards, P.P., V.L. Kuznetsov, and W.I. David, *Hydrogen energy.* Philos Trans A Math Phys Eng Sci, 2007. **365**(1853): p. 1043-56.
3. Vetrano, J.B., *Hydrides as neutron moderator and reflector materials.* Nuclear Engineering and Design, 1971. **14**(3): p. 390-412.

4. Sakintuna, B., F. Lamaridarkrim, and M. Hirscher, *Metal hydride materials for solid hydrogen storage: A review☆.* International Journal of Hydrogen Energy, 2007. **32**(9): p. 1121-1140.
5. Davies, N. and R. Forrester, *Effects of irradiation on hydrided zirconium-uranium alloy NAA 120-4 experiment*. 1970, Atomics International Div.: Canoga Park, CA.
6. Simnad, M., *The U-ZrHx alloy: Its properties and use in TRIGA fuel.* Nuclear Engineering and Design, 1981. **64**(3): p. 403-422.
7. Haslett, R., *Space Nuclear Thermal Propulsion Program*. 1995, Grumman Aerospace Corp.: Bethpage, NY.
8. Miller, A.J., *Aircraft Nuclear Propulsion Project Semiannual Progress Report.* ornl-2599, 1959.
9. Iwasaki, T. and K. Konashi, *Development of Hydride Absorber for Fast Reactor—Application of Hafnium Hydride to Control Rod of Large Fast Reactor—.* Journal of Nuclear Science and Technology, 2009. **46**(8): p. 874-882.
10. Anderson, J.L., W. Mayo, and E. Lantz, *Reactivity control of fast-spectrum reactors by reversible hydriding of yttrium zones.* 1968. **NASA TN D-4615**.
11. Shivprasad, A.P., et al., *Elastic moduli of high-density, sintered monoliths of yttrium dihydride.* Journal of Alloys and Compounds, 2020: p. 153955.
12. Van Houten, R., *Selected Engineering And Fabrication Aspects Of Nuclear Metal Hydrides (Li, Ti, Zr, And Y).* Nuclear Engineering and Design, 1974. **31**: p. 434-448.
13. Weinberg, A.M., *The First Nuclear Era: The Life and Times of a Technological Fixer.* Springer Science & Business Media, 1994.
14. *Rare Earths Statistics and Information.* National Minerals Information Center, United States Geological Survey, 2020.
15. Advanced Small Modular Reactors, Department of Energy. https://www.energy.gov/ne/nuclear-reactor-technologies/small-modular-nuclear-reactors.
16. Oak Ridge National Laboratory, *Transformational Challenge Reactor.* https://tcr.ornl.gov, 2019.
17. B.R. Betzler, B.J.A., A.J. Wysocki, P.K. Jain, P.C. Chesser, M.S. Greenwood, K.A. Terrani, *Transformational Challenge Reactor Preconceptual Core Design Studies.* Nuclear Engineering and Design, 2020. **Submitted**.
18. Van Houten, R., *Hydriding Process.* US3720751, 1973.
19. Van Houten, R., *Massive Metal Hydride Structures And Methods For Their Preparation.* US3720752, 1973.
20. Setoyama, D., et al., *Mechanical properties of yttrium hydride.* Journal of Alloys and Compounds, 2005. **394**(1-2): p. 207-210.
21. Ito, M., et al., *Thermal properties of yttrium hydride.* Journal of Nuclear Materials, 2005. **344**(1-3): p. 295-297.
22. Shivprasad, A.P., et al., *Development of sintered yttrium dihydride compacts for nuclear reactor moderator applications.* Nuclear and Emerging Technology for Space, American Nuclear Society Topical Meeting, 2019.
23. Hu, X., et al., *Fabrication of yttrium hydride for high-temperature moderator application.* Journal of Nuclear Materials, 2020. **539**: p. 152335.
24. Begun, G.M., J.F. Land, and J.T. Bell, *High temperature equilibrium measurements of the yttrium–hydrogen isotope (H_2, D_2, T_2) systems.* The Journal of Chemical Physics, 1980. **72**(5): p. 2959-2966.
25. Khatamian, D. and F.D. Manchester, *H-Y (Hydrogen-Yttrium).* Binary Alloy Phase Diagram, 1990. **2**: p. 2074-2075.
26. Fu, K., et al., *Experimental investigation and thermodynamic assessment of the yttrium-hydrogen binary system.* Progress in Natural Science: Materials International, 2018. **28**(3): p. 332-336.
27. Peng, J., et al., *Thermodynamic modelling of Y–H and Y–Zr–H system aided by first-principles and its application in bulk hydride moderator fabrication.* Journal of Nuclear Materials, 2020. **531**.
28. Lundin, C.E. and J.P. Blackledge, *Pressure-Temperature-Composition Relationships of the Yttrium-Hydrogen System.* Journal of The Electrochemical Society, 1962. **109**: p. 838-842.

29. Yannopoulos, L.N., R.K. Edwards, and P.G. Wahlbeck, *The Thermodynamics of the Yttrium-Hydrogen System.* The Journal of Physical Chemistry, 1965. **69**(8): p. 2510-2515.
30. Hu, X., K.A. Terrani, and B.D. Wirth, *Hydrogen desorption kinetics from zirconium hydride and zirconium metal in vacuum.* Journal of Nuclear Materials, 2014. **448**(1-3): p. 87-95.
31. Williamson, R.L., et al., *Multidimensional multiphysics simulation of nuclear fuel behavior.* Journal of Nuclear Materials, 2012. **423**(1-3): p. 149-163.
32. Ito, M., *Studies on Physical Properties of Metal Hydrides and Hydrogen Behavior in Zr Alloys.* Osaka University, 2008. **PhD Thesis**.
33. Larson, A.C. and R.B. Von Dreele, *General Structure Analysis System* Los Alamos National Laboratory Report LAUR 86-748, 2004.
34. ASTM E1269-11, *Standard Test Method for Determining Specific Heat Capacity by Differential Scanning Calorimetry*. 2018, ASTM International: West Conshohocken, PA.
35. ASTM E1461-07, *Standard Test Method for Thermal Diffusivity by the Flash Method*. 2007, ASTM International: West Conshohocken, PA.
36. Cowan, R.D., *Pulse Method of Measuring Thermal Diffusivity at High Temperatures.* Journal of Applied Physics, 1963. **34**(4): p. 926-927.
37. Clark III, L.M. and R.E. Taylor, *Radiation loss in the flash method for thermal diffusivity.* Journal of Applied Physics, 1975. **46**(2): p. 714-719.
38. Ptak, M., et al., *Experimental and theoretical studies of structural phase transition in a novel polar perovskite-like $[C_2H_5NH_3][Na_{0.5}Fe_{0.5}(HCOO)_3]$ formate.* Dalton Transactions, 2016. **45**(6): p. 2574-2583.
39. Ito, M., et al., *Thermal properties of yttrium hydride.* Journal of Nuclear Materials, 2005. **344**(1): p. 295-297.
40. Setoyama, D., et al., *Mechanical properties of yttrium hydride.* Journal of Alloys and Compounds, 2005. **394**(1): p. 207-210.
41. Ito, M., *Studies on Physical Properties of Metal Hydrides and Hydrogen Behavior in Zr Alloys. Osaka University*, in *Division of Sustanable Energy and Environmental Engineering*. 2008, Osaka University: Osaka.
42. Khatamian, D. and F.D. Manchester, *The H-Y (Hydrogen-Yttrium) System.* Bulletin of Alloy Phase Diagrams, 1988. **9**(3): p. 252-260.
43. Lundin, C.E. and J.P. Blackledge, *Pressure-Temperature-Composition Relationships of the Yttrium-Hydrogen System.* Journal of The Electrochemical Society, 1962. **109**(9): p. 838.
44. Beaudry, B.J. and F.H. Spedding, *The solubility of RH_{2-X} in Gd, Er, Tm, Lu and Y from ambient to 850°C.* Metallurgical and Materials Transactions B, 1975. **6**(3): p. 419-427.
45. Bonnet, J.E., C. Juckum, and A. Lucasson, *Solid solutions of H and D in yttrium metal.* Journal of Physics F: Metal Physics, 1982. **12**(4): p. 699-711.
46. Yannopoulos, L.N., R.K. Edwards, and P.G. Wahlbeck, *The Thermodynamics of the Yttrium-Hydrogen System1.* The Journal of Physical Chemistry, 1965. **69**(8): p. 2510-2515.
47. Landin, N.A., et al., *The Y-YH_2 Equilibrium Diagram at Room Temperature.* Russian Journal of Inorganic Chemistry, 1971. **16**: p. 274-276.
48. Udovic, T.J., Q. Huang, and J.J. Rush, *A neutron-powder-diffraction study of the rare-earth deuteride two-phase region.* Journal of Alloys and Compounds, 2003. **356-357**: p. 41-44.
49. Chiheb, M., J.N. Daou, and P. Vajda, *Lattice Parameters of the β-Phase Rare-Earth Hydrides Rh_{2+x} (R = Y, Gd, Tb, Dy).* International Journal of Research in Physical Chemistry & Chemical Physics, 1993. **179**: p. 255-260.
50. Kurosaki, K., et al., *The δ'/δ phase transition in hafnium hydride and deuteride.* Journal of Nuclear Science and Technology, 2015. **52**(4): p. 541-545.
51. Libowitz, G.G., *Nonstoichiometry in Metal Hydrides*, in *Nonstoichiometric Compounds*. 1963, American Chemical Society. p. 74-86.
52. Peterman, D.J., et al., *Electronic structure of metal hydrides. II. Band theory of ScH_2 and YH_2.* Physical Review B, 1979. **19**(10): p. 4867-4875.

53. Weaver, J.H., R. Rosei, and D.T. Peterson, *Electronic structure of metal hydrides. I. Optical studies of ScH_2, YH_2, and LuH_2.* Physical Review B, 1979. **19**(10): p. 4855-4866.
54. Anderson, D.L., et al., *Hydrogen location in yttrium dihydride by means of NMR measurements.* Physical Review B, 1980. **21**(6): p. 2625-2626.
55. Khatamian, D., et al., *Crystal structure of $YD_{1.96}$ and $YH_{1.98}$ by neutron diffraction.* Physical Review B, 1980. **21**(6): p. 2622-2624.
56. Goldstone, J.A., et al., *Temperature dependence of hydrogen site occupancy in Yttrium dihydride.* Solid State Communications, 1984. **49**(5): p. 475-478.
57. Parker, D.S., *USAEC Report APEX-588.* General Electric Company, 1960.
58. Nix, W.D. and H. Gao, *Indentation size effects in crystalline materials: A law for strain gradient plasticity.* Journal of the Mechanics and Physics of Solids, 1998. **46**(3): p. 411-425.
59. *Standard Practice for Instrumented Indentation Testing.* ASTM E2546 - 15.
60. Sudharshan Phani, P. and W.C. Oliver, *A critical assessment of the effect of indentation spacing on the measurement of hardness and modulus using instrumented indentation testing.* Materials & Design, 2019. **164**.